Journal Name

COMMUNICATION

Supplemental Information to:

Spatial selectivity of photodeposition reactions on polar surfaces of centrosymmetric ferroelastic γ-WO_3†

Ajay S. Pisat, Gregory S. Rohrer, and Paul A. Salvador*

Received 00th January 20xx,
Accepted 00th January 20xx

DOI: 10.1039/x0xx00000x

www.rsc.org/MaterialsA

This pdf document contains details of WO_3 sample preparation, x-ray diffraction, electron microscopy methods, identification of crystallographic orientation of domain boundaries, piezoforce microscopy, and photochemical marker reactions. It contains a table of polishing procedures (Table S1) and figures of: experimental and simulated x-ray diffraction patterns (Fig. S1), backscatter electron image of the multilevel domain structure and related crystallography (Fig. S2), schematic of photochemical marker reactions (Fig. S3), and examples of secondary electron images of Ag coated (Fig. S4 and S5) and PbO_2 or MnO_2 coated (Fig. S6) surfaces after photochemical marker reactions.

1. Preparation of γ-WO_3 samples

Commercial WO_3 powder (99.9%, Sigma Aldrich) was used throughout this work. The powder was wet ground in acetone using a mortar and pestle for 5 min. 2 g of ground powder was then mixed with a drop of polyvinyl alcohol as a binder and cold-pressed into a pellet using a tabletop hydraulic press (Carver). Pressed pellets were then sintered in an alumina crucible. The pellets were laid on a bed of WO_3 powder to prevent direct reaction with the alumina during sintering. The pellets were fired at 1100 °C for 4 h using a ramp rate of 10 °C/min for heating and cooling. On cooling, the pellets go through the α–β (740 °C) and β–γ (310 °C) transformations.

One side of a given pellet was polished to a mirror finish. Polishing was carried out on a Buehler Automet 250 machine, with a head cadence of 60 revolution per minute (rpm) and a force of 1 lb. Details of the polishing steps are given in Table S1. After polishing, the pellets were annealed at 600 °C for 1 h, heating at 5 °C/min and cooling at 10 °C/min, to heal polishing damage at the surface. It should be noted that this thermal cycling goes through the β–γ (310 °C) transformation. Prior to further surface analysis, polished pellets were sonicated successively in acetone, ethanol, and DI water for 3 min each.

Table S1: Recipe for polishing the sintered WO_3 pellets

Step number	Base speed[a]	Polishing paper/cloth + suspension	Time[a]
1	120	320 grit Carbimet	0.5
2	120	600 grit Carbimet	1
3	120	800 grit Carbimet	1.5
4	150	1200 grit Carbimet	2
5	180	Satyn MB + 9 µm diamond suspension	3
6	180	Satyn MB + 3 µm diamond suspension	4
7	180	Satyn MB + 1 µm diamond suspension	5
8	200	Micro MB + 0.05 µm diamond suspension	8

[a] Base speed is given in rpm and time in min.

2. X-ray Diffraction (XRD)

One polished pellet was ground using a mortar and pestle for x-ray diffraction (XRD) analysis. The powder was spread on a glass slide and mounted in an X'Pert Pro MPD x-ray diffractometer. XRD was carried out using 45 kV and 40 mA with a Cu target (radiation wavelength 1.54 Å). Θ-2Θ patterns were collected, registering XRD intensity every 0.026 ° from 20 – 65 ° at a speed of 0.067 °/s. An x-ray diffractogram for γ-WO_3 was simulated using CrystalDiffract[1] software for comparison with the acquired patterns. The structural parameters for γ-WO_3 were taken from Loopstra and Rietveld.[2]

In Fig. S1, the experimental XRD pattern is given as the upper curve and the simulated pattern is given as the lower curve. The number and position of peaks in the experimental pattern were well matched to peaks in the simulated pattern, though the relative intensities varied between peaks in the two patterns. The simulated pattern assumes a perfectly random mixture of orientations with identical grain sizes and shape, which is not likely true in the experimental powder. The similarity of the patterns (and the dis-similarity to other polymorphs, not shown) support the conclusion that the sample is γ-WO_3.

*Department of Materials Science and Engineering, Carnegie Mellon University, 5000 Forbes Ave., Pittsburgh, PA, 15213-3890, USA: Email: *Email - paulsalvador@cmu.edu*

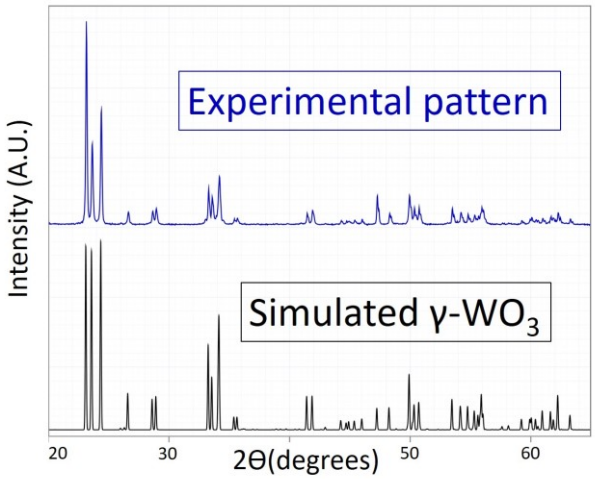

Fig. S1: Comparison of the experimental and simulated XRD patterns.

3. Backscatter electron (BSE) imaging

BSE imaging was carried out using an FEI Quanta 200 FEG (field emission gun) and an FEI Quanta 600 FEG scanning electron microscope (SEM). Accelerating voltages ranged from 5 to 15 kV. The spot size was typically 4 or 5, but 3.5 was used for improved imaging of tertiary domains. The contrast was set to 80-90 % of the maximum possible value while the brightness was set to 0-15 % of the maximum possible value. The image acquisition times ranged from 3-6 minutes per image to achieve the desirable quality (i.e., signal-to-noise ratio). Image resolution was 1024 x 884. Contrast between domains arises from differences between electron counts from differences in electron channeling in different domains.

Similar domain structures to those given in various figures throughout the main text and SI were observed for all grains. Primary and secondary domains were almost always evident, but tertiary domains were not consistently imaged. The tertiary domains are at the limit of the microscope's resolution and their appearance is sensitive to their local character and to imaging conditions. The lack of contrast from domains in a given BSE image does not rule out their presence. We did not concentrate on characterizing the tertiary domains.

4. Electron Backscatter Diffraction (EBSD)

EBSD was carried out using an FEI Quanta 600 FEG SEM equipped with an Oxford HKL EBSD system and an HKL NordlysNano camera. The accelerating voltage was 20 kV. The sample was mounted on a pre-tilted sample holder (70°). Patterns were collected using a dwell time between 140 and 200 ms per frame and averaging two frames together for the final pattern.

The patterns were then indexed using two variations of the space group No. 14: $P2_1/c$ and $P2_1/n$. In the $P2_1/c$ system, the cell parameters used were a = 7.69 Å, b = 7.54 Å, c= 10.525 Å and β = 136.05° (calculated from the P $2_1/n$ values given below). This setting was used to resolve crystallographic orientation differences for the secondary domains (shown in Fig. 2(b)). In the $P2_1/n$ system, the cell parameters were a = 7.36 Å, b = 7.54 Å, c = 7.69 Å and β = 90.9°.[2] This setting corresponds well to the (doubled) pseudo-perovskite unit cell, and we used it to simplify the categorization of the primary and secondary domain wall crystallography (which we describe relative to the cubic system below).

5. Identification of Domain walls

The observed domain structures (see main text) have two characteristic features: primary domains that span the length of the grain and secondary domains that span the width of their corresponding primary domain. The hierarchical structure suggests that the primary structure might form as a result of the α-WO_3 (tetragonal) to β-WO_3 (orthorhombic) transition that occurs when the sample is cooled below 740 °C after synthesis and that the secondary structure might form as a result of the β-WO_3 (orthorhombic) to γ-WO_3 (monoclinic) transition that occurs when the sample is cooled below 310 °C (on cooling from the post-polishing anneal).

To identify the crystallography associated to primary and secondary domain boundaries, we studied grains that had the *a*, *b*, or *c* axes oriented within 10° of the surface normal, based on the $P2_1/n$ EBSD data. The $P2_1/n$ monoclinic γ-WO_3 structure can be most easily understood as a distorted doubled perovskite with the A-sites completely empty.[3] Because all polymorphs can be related to the cubic pseudo-perovskite subcell, we used the data in the $P2_1/n$ setting to describe the crystallography. Fig. S2 shows a BSE image of a grain whose primary domains have the [100] or [010] axes normal to the surface plane. Below the image, the crystal axes are show for two domains (indicated by arrows).

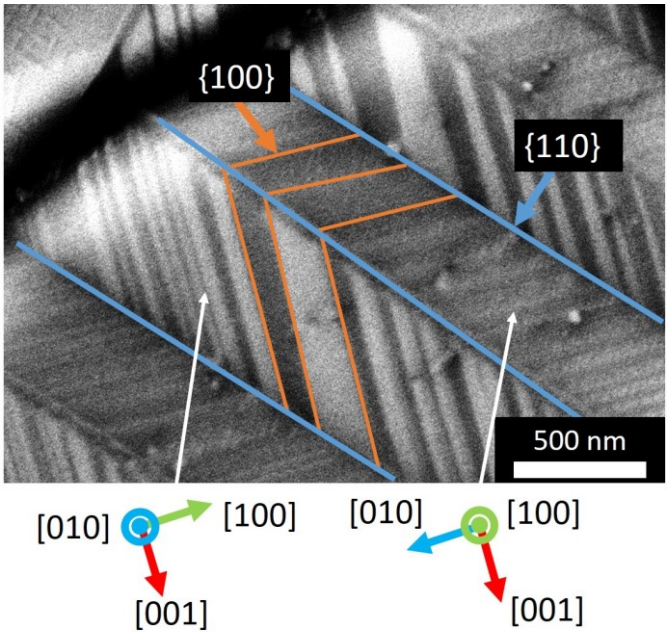

Fig. S2: BSE image of a grain showing two levels of domains. The Blue lines indicate the primary domain boundaries. The orange lines indicate the secondary domain boundaries. The orientations of the primary domains as indexed in the P $2_1/n$ (pseudo-perovskite) system are indicated by the coordinate systems shown below.

Using the Euler angles of the primary domains, we determined the angles that the traces of planes in the {110} and {100} families would make with the surface plane. The calculated traces were then matched with the observed traces using ImageJ.[4] The traces of the (-101) and (011) planes (according to the two different coordinate systems of the two different primary domains), are depicted in blue in Fig. S2 (marked as {110}). These align well with the primary domain boundaries. The traces of the (100) and (001) planes (according to the two different coordinate systems of the two different primary domains), are depicted in orange in Fig. S2 (marked as {100}). These align well with the secondary domain boundaries. The measured angle between the traces of the secondary domain boundaries is 90 ± 1°, consistent with the expected angle between the traces of the (100) and (001) planes.

Similar analyses were carried out for several grains. In the cases investigated, the primary domain boundaries were consistent with $\{110\}_p$ planes and the secondary boundaries with $\{100\}_p$ planes, where the subscript *p* denotes these are given using the cubic pseudo-perovskite indexes. Further, the rotation across the primary domains was usually 90° about the $<100>_p$ and the rotation about the secondary domains were 180 ° about another $<100>_p$ direction. These types of planes are commonly observed as domain boundaries in WO_3. [5-13]

Following Sapriel's[24] analysis suggests that domains formed as a result of the tetragonal to orthorhombic ferroelastic transition should have domain walls along x = y or x = -y. In γ-WO_3 terms, this means the domains associated with the α to β (tetragonal to orthorhombic) transformation could lie along the $\{110\}_p$ planes, which is consistent with the primary domain boundaries. Sapriel's[24] analysis also suggests that domains formed as a result of the orthorhombic to monoclinic ferroelastic transition should have domain boundaries along x=0 and z=0, which implies walls along (001) or (100), which are consistent with the secondary domains.

Thus, the primary domains, which span entire grains, are consistent with expectations from the α to β (tetragonal to orthorhombic) transition (at 740 °C).[5-10] The secondary and tertiary domains are consistent with the β to γ (orthorhombic to monoclinic) transition (at 310 °C).[5-13] These observations are also consistent with the domain boundary planes reported by Tanisaki[26] on single crystals of WO_3.

6. Piezoforce Microscopy (PFM)

Piezoforce Microscopy (PFM) was carried out using an NT-MDT Solver NEXT tabletop AFM. The samples were cleaned in acetone, ethyl alcohol, and distilled water, and then wiped with a methanol soaked Kimwipe (KimTech) before being imaged in the AFM. Conductive probes by Nanoworld (ARROW-EFM: cantilever frequency = 75 kHz, spring constant = 2.8 N/m, cantilever length = 240 µm) were used. A scanning speed of 3 µm/s was used, with an AC bias of 4 V. The AC frequency used was approximately 320 kHz, where the first contact resonance was observed. As described in the main text, the PFM contrast correlated well with the primary and secondary domain structures. We did not resolve if (or how) the surface polarity was related to the tertiary domain structure.

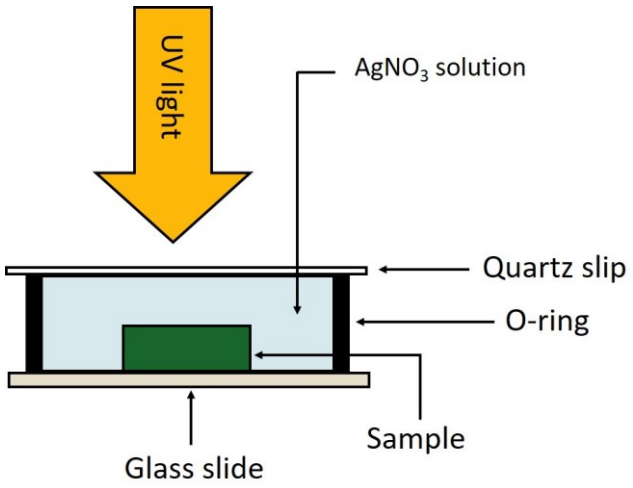

Fig. S3: Schematic of the setup for carrying out photochemical marker reactions.

7. Photochemical Ag^+ reduction

The setup used for photodeposition reactions (the marker reactions) is schematized in Fig. S3. The sample was attached to a glass slide using double sided tape. A rubber O-ring was placed upon the glass slide surrounding the sample. An appropriate solution was filled up to the brim of the O-ring, which was then covered with a thin quartz slip. The quartz slip was used to allow complete transmission of UV light while retaining the solution within the O-ring. For Ag^+ reduction, a 0.115 M solution of $AgNO_3$ was used, prepared by dissolving 0.097 g of $AgNO_3$ in 5 ml of distilled water. For Pb^{+2} (Mn^{2+}) photo-oxidation, a 0.345 M solution of $Pb(CH_3COO)_2$ (0.345 M solution of $MnSO_4$-$4H_2O$) was used, prepared by dissolving 0.561 g of $Pb(CH_3COO)_2$ (0.384 g of $MnSO_4$-$4H_2O$) in 5 ml of distilled water.

The Ag^+ photoreduction (Pb^{2+}/Mn^{2+} photo-oxidation) reactions were carried out by exposing the above setup to UV light with a power of 75 W for 6 s (150 W for 180 s). The incident UV light excites electrons in the sample to the conduction band, leaving holes in the valence band. The photogenerated carriers move to the solution-sample interface where one carrier reacts with the metal ions to form water-insoluble deposits of Ag, PbO_2, or MnO_2, while the other carrier reacts with water. After photochemical reaction, the sample was cleaned of excess solution by carefully dipping it in distilled water 10 times. The sample surface was then dried using a 99.99 % pure nitrogen stream.

Secondary electron (SE) imaging of samples after marker reactions was carried out using the FEI Quanta 600 at 20 kV with a spot size of 4. The acquisition time for each image was 3-6 min. Longer times were necessary to image finer silver particles (sizes ≈ 50 nm) on domains. SE images are given in Figs S4, S5, and S6.

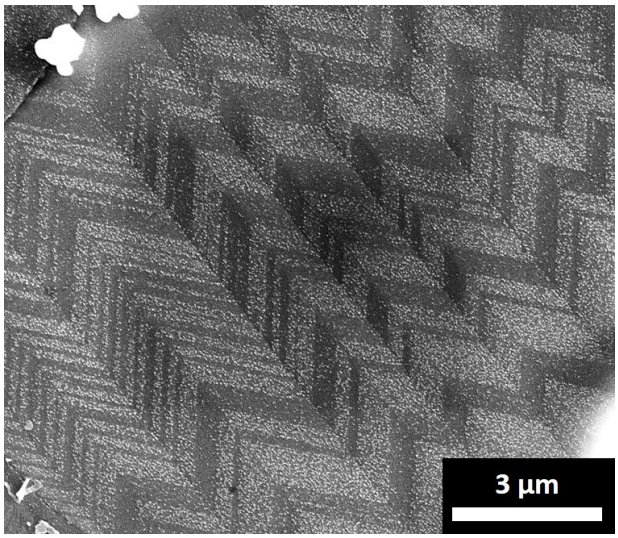

Fig. S4. An SE image of domain specific photochemical Ag^{+} reduction on the surface of the WO_3.

The topographic contrast from deposited particles shows up as bright contrast in Figs S4, S5, and S6. The contrast from Ag particles is overlaid on the weaker crystallographic contrast (see main text), the latter of which is more readily observable in Fig. S5 (at the higher magnification). The patterns of deposited Ag in Fig. S4 and S5 correlate with the secondary domain patterns as observed in BSE, EBSD, and PFM images given in the main text and SI. In Fig. S4, clear chevron patterns are observed, with some secondary domains covered densely with Ag particles and others covered sparsely. In Fig. S5, four bright primary domains (that run up and to the left at a shallow angle) are more reactive than the four dark domains. Within the reactive primary domain, the silver particles seem to be ordered into lines (that run up and to the left at a steep angle). These lines traverse the primary domains in a similar pattern to the expectation of secondary domains.

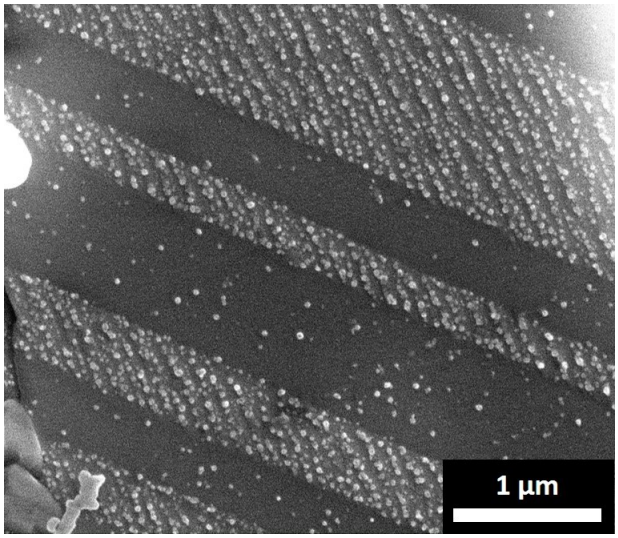

Fig. S5. An SE image of domain specific photochemical Ag^{+} reduction on the surface of the WO_3.

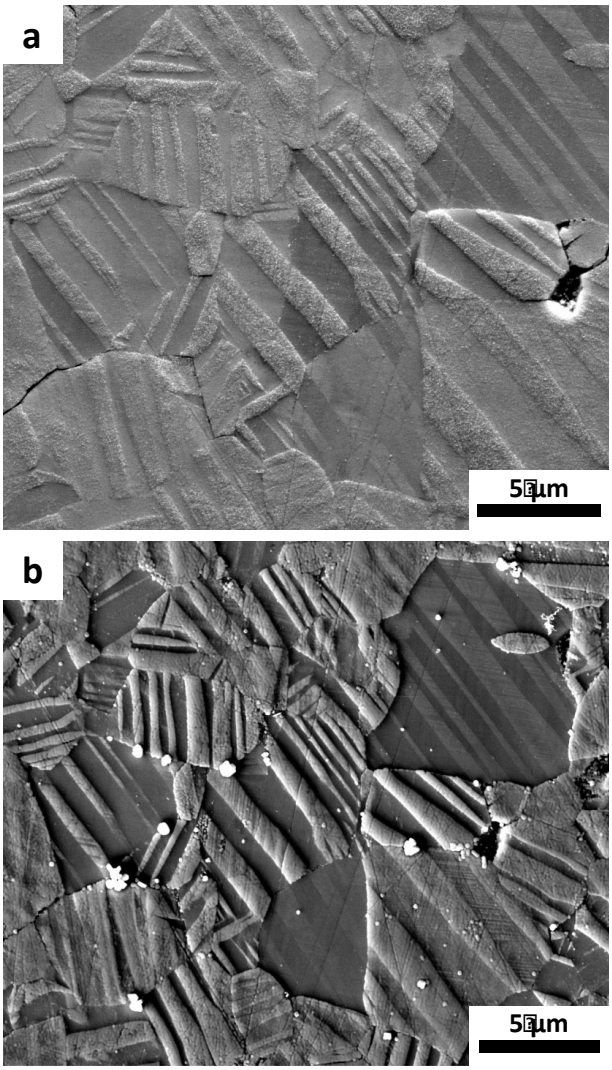

Fig. S6. SE image of domain specific photochemical oxidation of (a) Mn^{2+} and (b) Pb^{2+} on the surface of the WO_3.

Photo-oxidation of Pb^{2+} and Mn^{2+} to insoluble PbO_2 and MnO_2 were also carried out on the WO_3 surfaces. SE images after Mn^{2+} and Pb^{2+} oxidation are shown in Fig. S6(a) and (b), respectively. The patterns of photodeposited products in Fig. S6 again correlate with the secondary domain patterns as observed in BSE, EBSD, and PFM images given in the main text and SI, indicating that oxidation reactions are also correlated with the ferroelastic domain structure of WO_3, especially the primary and secondary domains. An example of complementary reactivity on WO_3 is shown in Fig. 5 of the main text.

Notes and references

1 Simulated XRD patterns were generated using CrystalMaker® (v.9) and CrystalDiffract® (v.6). http://www.crystalmaker.com/ , http://crystalmaker.com/crystaldiffract/, 2016).
2 B. O. Loopstra and H. M. Rietveld, *Acta Crystallographica B*, 1969, **25**, 1420-1421.
3 T. Vogt, P. M. Woodward and B. A. Hunter, *J. Solid State Chem.*, 1999, **144**, 209-215.

4 C. A. Schneider, W. S. Rasband and K. W. Eliceiri, *Nat Methods*, 2012, **9**, 671-675.
5 R. Ueda and T. Ichinokawa, *J. Phys. Soc. Jpn.*, 1951, **6**, 122-123.
6 R. G. Rhodes, *Nature*, 1952, **170**, 369-369.
7 J. A. Perri, E. Banks and B. Post, *J. Appl. Phys.*, 1957, **28**, 1272-1275.
8 S. Tanisaki, *J. Phys. Soc. Jpn.*, 1958, **13**, 363-366.
9 S. Sawada and G. C. Danielson, *Phys. Rev.*, 1959, **113**, 1005-1008.
10 J. Sapriel, *Phys. Rev. B*, 1975, **12**, 5128-5140.
11 S. Hamazaki, N. Tashiro, F. Shimizu and M. Takashige, *J. Phys. Soc. Jpn.*, 1998, **67**, 2144-2145.
12 S. Hamazaki, N. Tashiro, F. Shimizu, S. Sawada and M. Takashige, *Ferroelectrics*, 1999, **231**, 631-635.
13 S. Yun, C. S. Woo, G. Y. Kim, P. Sharma, J. H. Lee, K. Chu, J. H. Song, S. Y. Chung, J. Seidel, S. Y. Choi and C. H. Yang, *Appl. Phys. Lett.*, 2015, **107**.